ISSN 2683-345X
journal homepage: http://ijiemjournal.uns.ac.rs/

International Journal of Industrial Engineering and Management

2026 / ARTICLE-IN-PRESS / 420

Original research article

Digital Twin-Enabled Decision Support Framework for Tailings Dam Operations and Safety

Hussein A. Saleem[a,b,*] 0000-0003-3955-9090

[a] *Mining Engineering Department, King Abdulaziz University Jeddah, Jeddah 21589, Saudi Arabia;*

[b] *Mining and Metallurgical Engineering Department, Faculty of Engineering, Assiut University, Assiut 71515, Egypt*

ABSTRACT

Tailings storage facilities deal with urgent decisions amid unsure water and strength conditions. This study presents a digital twin–enabled decision support framework that connects live sensing, physics-based simulation, and clear decision rules to support safe and open operations. The goal is to design and test a closed-loop workflow that changes monitoring signals into suggestions for water release and deposition scheduling. The framework links a sensor-instrumented 1:60 physical model of a downstream-raised dam with a matched numerical model. State estimation applies a Kalman filter. Seepage and stability get solved with Richards flow and limit-equilibrium analysis. Scenario tests include routine operation, heavy rainfall, and a quick-load case. A weighted cost function balances safety standards, pond goals, and production changes to pick actions. Compared to a rule-based baseline, the framework reduced time to first action from 34 to 21 minutes, increased the minimum factor of safety from 1.28 to 1.36, and decreased peak pond level from 0.33 to 0.29 m. State estimation errors for pond level and pore pressure stayed small. The framework moves operations from reactive checks to proactive control, with water balance acting as the key tool. The method's new aspect is the closed loop that combines sensing, hydro-mechanical simulation, and direct action in one workflow. In practice, sites should start early pond release and short-term deposition cuts as the factor of safety nears about 1.35, and combine seepage-stability modeling with Kalman-filtered monitoring to make decisions quick and trackable.

ARTICLE INFO

Article history:

Received January 26, 2026
Revised April 23, 2026
Accepted May 5, 2026
Published online June 26, 2026

Keywords:
Decision support;
Digital twin;
Hydro-mechanical modeling;
Tailings dam;
Water balance

*Corresponding author:
Hussein A. Saleem
HASaleem1@outlook.com

1. Introduction

Tailings dams store mining waste and directly link industrial production with public and environmental safety [1]. Despite advances in engineering and regulation, recent global evidence shows that major failures continue to occur, often with severe and long-lasting consequences [1], [2]. Studies of historical failures indicate that such events rarely stem from a single cause; instead, they emerge from interacting factors such as water management, construction practices, and operational decisions over time [3]. These complexities highlight the importance of proactive and well-informed management.

Operating a Tailings Storage Facility (TSF) requires continuous decision-making regarding pond levels, discharge timing, and deposition rates under uncertainty related to weather conditions, seepage, and material behavior [4], [5]. In practice, many operations still depend on periodic inspections and expert judgment, which can delay response times and limit the ability to act on rapidly evolving risks. This creates a clear need for forward-looking decision-support systems that enhance safety, improve operational efficiency, and ensure accountability in

Published by the University of Novi Sad, Faculty of Technical Sciences, Novi Sad, Serbia.

https://doi.org/10.24867/IJIEM-420

decision processes [6]. At the same time, regulatory frameworks such as the Global Industry Standard on Tailings Management (GISTM) are increasing demands for transparency, continuous monitoring, and auditable decision-making across the facility lifecycle [7]. Within Industry 4.0 and 5.0 paradigms, Digital Twin (DT) technologies offer a promising approach to meet these requirements by integrating real-time data, simulation, and decision logic into a unified system [8]-[10].

In response to these challenges, this study proposes a digital twin–based decision support framework for TSF operations [11]-[14]. The framework integrates real-time monitoring, scenario-based simulation, and rule-based decision-making into a closed-loop system that supports timely and traceable operational actions. The study addresses the following research questions: *Can a DT effectively combine real-time monitoring with physics-based simulation to generate actionable recommendations? How can scenario-based simulations improve water management and deposition decisions under extreme conditions? What decision rules and safety criteria ensure that recommendations are transparent and defensible?* To answer these questions, the study develops and evaluates a DT-based framework with the following objectives: (1) Develop a DT architecture linking live TSF sensor data with stability and water balance models. (2) Implement a decision-support module that evaluates scenarios and recommends actions based on safety criteria. (3) Test the framework through scenario analysis comparing DT-guided and conventional operations. (4) Assess improvements in decision timeliness, safety, and operational efficiency.

2. Literature Review

Research on tailings dam safety spans several key domains. One major stream focuses on failure databases and forensic analyses, which identify recurring failure mechanisms and systemic weaknesses [15]-[16]. These studies consistently show that failures remain a persistent risk and that relying solely on historical patterns is insufficient for real-time decision-making. A second stream develops formal risk assessment frameworks, including tailored risk matrices for TSFs [17]-[19]. While these approaches provide structured evaluation tools, they are often static and heavily dependent on expert judgment, limiting their responsiveness to changing operational conditions. A third body of work applies physics-based modeling to assess dam stability and seepage behavior [20]-[24]. These models capture the interaction between material properties and hydraulic conditions, offering valuable insights into safety margins. However, they are typically used in periodic assessments rather than continuous operational support, which reduces their practical utility in dynamic environments. A fourth research stream emphasizes monitoring and early warning systems [25]-[27]. Technologies such as Interferometric Synthetic Aperture Radar (InSAR) enable high-resolution detection of ground deformation, while integrated systems combine satellite data, in-situ sensors, and remote sensing techniques [28]. Advances include time-series analysis, hybrid monitoring approaches, and visualization platforms for operators [29]. Despite these developments, translating monitoring signals into actionable decisions remains a key challenge, particularly under uncertainty and rapidly changing conditions.

Differences in spatial and temporal resolution across monitoring systems further complicate interpretation [30]. Satellite-based methods provide broad coverage but may miss short-term variations, whereas local sensors capture high-frequency data at limited points [31]. Efforts to integrate monitoring with numerical models demonstrate the potential of data fusion but also reveal sensitivity to assumptions about material properties and boundary conditions [32]. These limitations contribute to uncertainty in defining reliable alert thresholds and increase the risk of false or missed alarms [33].

DT research offers a promising integrative framework [34], [35]. A DT represents a dynamic virtual replica of a physical asset, continuously updated with real-time data and capable of supporting simulation and decision-making [36]. Unlike static models, DTs emphasize continuous data assimilation, model updating, and scenario exploration [37]. In high-risk infrastructures, this enables testing of operational strategies under shared assumptions, improving both responsiveness and transparency [38]. However, the effectiveness of DTs depends on their ability to handle uncertainty and support bidirectional interaction between physical and digital systems [39]. Conceptual distinctions between digital models, digital shadows, and full DTs highlight the importance of feedback loops for operational control [40]. In civil engineering applications, DTs have been explored for maintenance, monitoring, and risk management, with demonstrated benefits but also persistent challenges related to uncertainty quantification and lifecycle integration [37]. Despite these advances, applications of DTs in tailings dam operations remain limited. Existing approaches often focus on monitoring or

simulation in isolation, without fully integrating them into decision-support workflows tailored to TSF-specific challenges such as water balance management, deposition planning, and emergency response. The literature therefore reveals several gaps:

- Limited integration between monitoring data, simulation models, and operational decision-making.
- Lack of real-time, actionable guidance for operators under uncertainty.
- Insufficient adaptation of DT concepts to TSF-specific operational constraints.

The proposed framework addresses these gaps by integrating sensor data ingestion, state estimation (e.g., via Kalman filtering), hydro-mechanical simulation, and a rule-based decision module into a unified, auditable loop. This architecture enables continuous alignment between observed conditions, predicted behavior, and operational actions, distinguishing it from conventional monitoring dashboards and periodic assessments.

3. Methodology

3.1 Research Design and Experimental Setting

This study used a cyber-physical design [41]. This design connects a prototype tailings dam with sensors to a DT and a decision support layer. This study met the first goal. It built the DT setup for a TSF. It built a smaller physical system. It added instruments to it. It made a matching numerical model. This study met the second goal. It added decision support. It set clear rules for operations. It linked model results to specific guidelines and best choices. This study met the third goal. It tested the setup in typical cases. It ran controlled tests. These tests copied normal tasks and harsh conditions. This study met the last goal. It checked the benefits for operations. It compared choices and results with and without DT help. It used statistical tests and measures of impact for this. This setup made sure each method step backed a clear goal. It also kept data, models, and choices in line.

3.2 Experimental facility and physical prototype

This study built the physical prototype in a controlled laboratory environment. This step ensured consistent boundary conditions and safe operation. The model represented a downstream-raised tailings embankment at a geometric scale of 1:60. The crest length was 1.8 m. The crest width was 0.25 m. The maximum height was 0.9 m. The upstream and downstream slopes were 3H:1V and 2.5H:1V, respectively. A drainage layer of graded sand was at the base. This layer simulated under-drainage. A starter dam formed with compacted sandy silt. Tailings lifts were in 0.05 m layers. These layers mimicked staged deposition.

The tailings analog was a mixture of silica sand, kaolinite, and silt. This mixture matched the target particle size distribution and plasticity typical of metal mine tailings. The mixture was at a gravimetric water content of 18 percent. This content resulted in a saturated density near 1.75 g/cm^3 after compaction. Each lift compacted with a standardized energy. This energy maintained uniform density and reduced variability in stiffness. The upstream pond formed by controlled water addition. The pond margin stayed to match operational drawdown and recharge cycles. The prototype allowed direct observation of pore pressure and deformation changes during deposition and rainfall loading. It stayed small enough for controlled repeatability.

3.3 Instrumentation and data acquisition

The physical prototype served as a laboratory-scale demonstrator. It tested DT data assimilation and decision logic. The prototype had instruments. These tracked hydraulic and mechanical responses. These responses drive operational decisions. Pore water pressure was measured using vibrating wire piezometers. These were along the phreatic surface and the downstream toe. Settlement tracked with linear displacement transducers at the crest and mid-slope. Lateral deformation captured using a fiber Bragg grating inclinometer. This inclinometer has been shown to provide stable measurements in tailings dam contexts [41], [42]. Pond level measured with a pressure transducer in a stilling well. A rainfall simulator and a tipping-bucket gauge provided controlled precipitation inputs.

Sensors connected to a centralized data logger. It had a 1 min sampling rate for water level and rainfall. It had a 5 min rate for pore pressure and deformation. Data transmitted to the DT through a local network. This ensured low latency. This instrumentation strategy followed the architecture of recent tailings monitoring systems. These systems combine multi-sensor data for early warning and operational support [43]. The sampling schedule balanced temporal resolution with data storage constraints. It allowed the DT to respond to rapid changes.

3.4 Calibration, data quality, and synchronization

All sensors were calibrated before testing, and a re-check was carried out after each scenario to verify stability. The linear calibration model is given by Equation (1).

$$x_{\text{true}} = a_0 + a_1 x_{\text{raw}} \tag{1}$$

where x_{raw} is the sensor output, x_{true} is the calibrated value, and a_0 and a_1 are calibration coefficients from least-squares fitting. Calibration was applied to each channel, and coefficients were updated if drift exceeded 1 percent over a 24 h period. This equation was implemented in the data pipeline before any model updating. It ensured that all DT inputs reflected physical units and that the decision module operated on consistent measurements.

The system synchronized time with a single reference clock in the data logger. A drift check compared timestamps to a local network time source at the start and end of each run. The process found outliers with a rolling median filter that had a 5-sample window. It filled in missing values with linear interpolation when gaps lasted less than 10 minutes. Longer gaps caused a scenario restart to keep data intact. This method made sure the DT got reliable and coherent input streams for state estimation.

3.5 Digital twin architecture and data integration

The team organized the DT into three layers: data acquisition and storage, hydro-mechanical simulation, and decision support. The architecture aligns with recent DT frameworks for civil infrastructure. Those frameworks stress continuous data synchronization and model updating [35]. The system followed cyber-physical design principles. Developers use these principles in DT development. In this approach, the physical asset and the virtual model link tightly through automated data flow [21]. The state variables included pond water level, phreatic surface elevation, pore pressure at each sensor location, and crest displacement. The model represented state evolution with the linear state-space form. Equation (2) shows this form.

$$\begin{aligned} \mathbf{x}_{k+1} &= \mathbf{A}\mathbf{x}_k + \mathbf{B}\mathbf{u}_k + \mathbf{w}_k \\ \mathbf{y}_k &= \mathbf{H}\mathbf{x}_k + \mathbf{v}_k \end{aligned} \tag{2}$$

where $\mathbf{x}_k$ is the state vector at time step k, $\mathbf{u}_k$ is the control input vector representing operational actions, $\mathbf{y}_k$ is the measurement vector, and $\mathbf{A}$, $\mathbf{B}$, and $\mathbf{H}$ are system matrices. The vectors $\mathbf{w}_k$ and $\mathbf{v}_k$ represent process and measurement noise. This equation structured how real-time data, operational actions, and model dynamics were linked. It served as the foundation for updating the DT and for propagating the effects of proposed decisions. State updates were performed with a Kalman filter [44], [45]. The update step is given by Equation (3).

$$\begin{aligned} \mathbf{K}_k &= \mathbf{P}_{k|k-1}\mathbf{H}^{\mathrm{T}}\left(\mathbf{H}\mathbf{P}_{k|k-1}\mathbf{H}^{\mathrm{T}} + \mathbf{R}\right)^{-1} \\ \mathbf{x}_{k|k} &= \mathbf{x}_{k|k-1} + \mathbf{K}_k\left(\mathbf{y}_k - \mathbf{H}\mathbf{x}_{k|k-1}\right) \\ \mathbf{P}_{k|k} &= \left(\mathbf{I} - \mathbf{K}_k\mathbf{H}\right)\mathbf{P}_{k|k-1} \end{aligned} \tag{3}$$

where $\mathbf{K}_k$ is the Kalman gain, $\mathbf{P}_{k|k\text{-}1}$ is the predicted error covariance, $\mathbf{P}_{k|k}$ is the updated covariance, $\mathbf{R}$ is measurement noise covariance, and $\mathbf{I}$ is the identity matrix. This update step merged sensor data with model predictions at each time step. It reduced noise sensitivity and improved the stability of subsequent simulations. The filtered state was then used to evaluate safety margins and to generate decision recommendations.

3.6 Hydro-mechanical modeling

Seepage and stability were modeled using coupled hydro-mechanical equations, consistent with recent reviews of dam seepage modeling [22]. The governing flow equation used the mixed-form Richards equation, shown in Equation (4).

$$\frac{\partial \theta}{\partial t} = \nabla \cdot \left[K(\theta)\left(\nabla h + \nabla z\right)\right] + S \tag{4}$$

where θ is volumetric water content, t is time, $K(\theta)$ is hydraulic conductivity, h is pressure head, z is elevation head, and S is a sink or source term that accounts for drainage and water addition. This equation was solved on a two-dimensional cross-section of the dam using a finite element mesh that was refined near the phreatic surface. It provided time-dependent pore pressure fields for each scenario. The soil-water retention relationship used a van Genuchten form, given in Equation (5).

$$\begin{aligned} \theta(h) &= \theta_{\mathrm{r}} + \frac{\theta_{\mathrm{s}} - \theta_{\mathrm{r}}}{\left(1 + (\alpha\,|\,h\,|)^n\right)^m} \\ m &= 1 - \frac{1}{n} \end{aligned} \tag{5}$$

where θ_{r} is residual water content, θ_{s} is saturated water content, α and n are fitting parameters, and m is a derived parameter. These parameters were obtained

from laboratory tests on the tailings analog. The retention curve linked pressure head to moisture content within the seepage model and allowed the DT to capture unsaturated behavior during drawdown and rainfall. Boundary fluxes were computed using Darcy's law, shown in Equation (6).

$$\mathbf{q} = -K(\theta)\left(\nabla h + \nabla z\right) \tag{6}$$

where $\mathbf{q}$ is the specific discharge vector and the remaining terms follow Equation (4). This equation provided seepage flux at the downstream face and the drainage layer. It was used to compute outflow for the pond water balance and to verify that boundary conditions in the numerical model were physically consistent. The flux values also served as inputs to the decision module for evaluating discharge actions. Shear strength was evaluated using the Mohr-Coulomb criterion, given in Equation (7).

$$\tau_{\mathrm{f}} = c' + \left(\sigma_{\mathrm{n}} - u\right)\tan\phi' \tag{7}$$

where τ_{f} is shear strength at failure, c' is effective cohesion, σ_{n} is normal stress, u is pore water pressure, and ϕ' is effective friction angle. Parameters were obtained from consolidated drained triaxial tests on the tailings analog. This equation linked pore pressure outputs to mechanical resistance and served as the basis for stability calculations under each scenario. Slope stability was assessed using a limit equilibrium approach consistent with tailings dam stability analyses [23]. The factor of safety is given by Equation (8).

$$F_{\mathrm{S}} = \frac{\sum_{i=1}^{n}\left[c'_i b_i + \left(W_i - u_i b_i\right)\tan\phi'_i\right]}{\sum_{i=1}^{n} W_i \sin\alpha_i} \tag{8}$$

where F_{S} is the factor of safety, n is the number of slices, b_i is slice width, W_i is slice weight, u_i is pore pressure at the base of slice i, and α_i is the base inclination. This equation was solved iteratively because F_{S} appears on both sides in Bishop-type methods. The resulting safety margin was a primary input to the decision support layer, which prioritized actions when F_{S} approached critical thresholds.

The failure mechanism that the DT is explicitly protecting against in this study is rainfall- and drawdown-driven slope instability of the downstream-raised embankment, in which a rising phreatic surface and elevated mid-slope pore pressure progressively reduce effective stress along potential slip surfaces and lower the limit-equilibrium factor of safety. Static liquefaction and internal erosion (piping) are recognized as additional failure modes for tailings dams, but the prototype geometry and instrumentation in this work are not configured to resolve their triggering criteria, and they are therefore treated as outside the scope of the present DT. The factor of safety is the primary, but not sole, proxy for failure proximity. The decision logic also monitors a deformation guardrail, defined as the rate of crest settlement and the cumulative inclinometer-based lateral displacement, and any exceedance of these instrumentation-based thresholds independently triggers the rapid-load intervention sequence even when the calculated factor of safety has not yet reached the critical value. This dual hydromechanical and kinematic trigger reduces the risk that a single proxy could mask an evolving failure mode.

3.7 Scenario design and operational inputs

The study designed scenario testing to cover normal work and possible problems. The research defined three operational modes. The first mode used routine deposition with stable water levels. The second mode looked at heavy rain where pond levels rose quickly. The third mode used a rapid load case. This case mimics an earthquake because it lowers shear strength for a short time. It must be emphasized, however, that the rapid-load case is an engineering approximation of the transient dynamic response of the embankment, not a fully resolved seismic simulation. The loading cycle reproduces a short, monotonic excess pore-pressure pulse and an associated transient reduction in available shear strength, which captures the dominant pathway by which a brief dynamic disturbance perturbs the factor of safety. It does not reproduce ground-motion frequency content, cyclic stress-strain hysteresis, site-amplification effects, or post-shaking liquefaction triggering analyses, all of which would require coupled dynamic effective-stress modelling outside the scope of this prototype study. The rapid-load scenario is therefore retained as a stress-test of the closed-loop decision logic under a sudden, transient strength reduction rather than as a substitute for a formal seismic stability assessment.

Each mode had three boundary conditions. These conditions changed based on rain intensity and the rate of deposition. This plan created nine main scenarios. The experimenters repeated each scenario twice. This didn't just check if the results were consistent. It also lowered the impact of random changes. These steps led to 18 experimental runs.

This sample size balanced the need for variety with the time needed for the system to stabilize be-

tween tests. The project updated pond levels with the water balance in Equation (9).

$$V_{t+\Delta t} = V_t + \left(Q_{\text{in}} - Q_{\text{out}} + PA_{\text{pond}} - EA_{\text{pond}} - I\right)\Delta t \quad (9)$$

where V_t is pond volume at time t, Q_{in} and Q_{out} are inflow and outflow rates, P is rainfall intensity, E is evaporation rate, A_{pond} is pond area, and I is infiltration loss to the tailings. This equation was discretized with a 1 min time step to match sensor sampling. It allowed the DT to translate rainfall and discharge actions into updated pond levels and to evaluate whether the operating envelope was exceeded.

Researchers designed rainfall patterns to match low and high intensity storms in dry climates. The low-intensity pattern matched short storms. The high-intensity pattern matched longer storms with more total rain. The study applied the same rain data to both the physical model and the DT. This kept the starting conditions the same. Controlled slurry addition showed how the material settled. The test kept the water level in each layer the same. This didn't let the permeability change too much.

3.9 Decision support and optimization logic

Operational actions were assessed through a weighted decision function that balances safety and operational efficiency. The cost function is given by Equation (10).

$$J = w_1\left(\frac{h - h_{\text{target}}}{h_{\max}}\right)^2 + w_2\left(\frac{1}{F_{\text{S}}}\right)^2 + w_3\left(\frac{D}{D_{\max}}\right)^2 \quad (10)$$

where J is the decision cost, h is pond level, h_{target} is the preferred operating level, $h_{\max}$ is the maximum allowable level, F_{S} is the factor of safety, D is deviation from the planned deposition rate, $D_{\max}$ is the allowable deviation, and w_1, w_2, and w_3 are weights that sum to one. The weights were selected through sensitivity testing to prioritize safety while preserving production continuity. This function was evaluated for each candidate action, and the minimum-cost action was recommended. A probability-of-failure mapping was used to translate safety margins into risk scores for decision ranking. The mapping is given by Equation (11).

The weighting scheme operationalizes the trade-off between safety, hydraulic operating envelope, and production continuity. The safety weight was set highest, followed by the pond-level weight and then the deposition-deviation weight, so that any candidate action that reduced the factor of safety could only be selected if the combined hydraulic and production gains were large enough to offset the safety penalty. Each term is normalized by its tolerable deviation, which places all three contributions on a dimensionless zero-to-one scale and avoids implicit weighting by unit choice. The weights are not site-invariant. They are treated as configurable policy parameters that should be retuned to the site-specific risk appetite. In a high-seismicity setting the safety weight would be increased to penalize factor-of-safety reductions more aggressively; in a high-rainfall setting the pond-level weight would be raised to push discharge actions earlier in the event; and in a reclamation-phase facility with diminished production pressure the deposition-deviation weight would be reduced. A structured sensitivity analysis was used in this study to identify a weight combination that was stable under the tested scenarios, and Section on Uncertainty and Sensitivity reports the resulting coefficients.

$$P_{\text{fail}} = \frac{1}{1 + \exp\left[-a\left(F_{\text{S}} - b\right)\right]} \quad (11)$$

where P_{fail} is the mapped failure probability, a controls the slope of the transition, and b sets the midpoint where P_{fail}=0.5. The parameters a and b were set using sensitivity tests so that small reductions in F_{S} produced meaningful risk changes without generating spurious alarms. This mapping aligned with risk-based decision approaches used in dam safety management [24]. It provided a common scale for comparing actions across different scenarios and supported transparent decision justification.

3.10 Validation, performance metrics, and statistical analysis

Model validation compared DT predictions with observed prototype measurements for pore pressure, pond level, and crest displacement. The primary error metric was the root mean square error defined by Equation (12).

$$\text{RMSE} = \sqrt{\frac{1}{N}\sum_{i=1}^{N}\left(y_i - \hat{y}_i\right)^2} \quad (12)$$

where y_i is the observed value, $\hat{y}_i$ is the DT prediction, and N is the number of observations in a scenario. RMSE was computed for each sensor type and each scenario to check for systematic bias. Acceptable performance was defined as RMSE below 10 percent of the observed range for each variable. These thresholds were used to confirm that the DT could support operational decisions with adequate fidelity.

Statistical comparisons of decisions with and without DT guidance used paired tests because each scenario was repeated under both conditions. Normality was assessed using the Shapiro-Wilk test, and a paired t-test or Wilcoxon signed-rank test was used accordingly. Effect size was quantified using Cohen's *d*, given by Equation (13).

$$d = \frac{\bar{x}_1 - \bar{x}_2}{s_p}$$
$$s_p = \sqrt{\frac{(n_1-1)s_1^2 + (n_2-1)s_2^2}{n_1 + n_2 - 2}} \quad (13)$$

where $\bar{x}_1$ and $\bar{x}_2$ are the mean outcomes for baseline and DT-guided decisions, s_1 and s_2 are standard deviations, n_1 and n_2 are sample sizes, and s_p is the pooled standard deviation. This effect size quantified practical improvement in response time and safety margin beyond statistical significance. Results were reported with two-sided *p*-values and 95 percent confidence intervals. This analysis ensured that reported gains were both statistically and operationally meaningful.

3.11 Uncertainty and sensitivity analysis

The study handled parameter uncertainty with a Monte Carlo method. This method changed hydraulic conductivity, cohesion, and friction angle within ranges from lab tests. Each scenario used 500 random runs. These runs gave a steady estimate of prediction ranges for pond level and factor of safety. The study checked sensitivity by calculating standardized regression coefficients between input parameters and main outputs. These coefficients showed that hydraulic conductivity and pond level had the biggest effect on safety margin during heavy rain. The study applied these uncertainty analyses to set the weights in the decision cost function. It also used them to find where extra monitoring would cut risk the most.

The uncertainty treatment explicitly distinguishes measurement uncertainty from model-parameter uncertainty. Measurement uncertainty was quantified from the sensor calibration and drift metrics reported in Table 1 and was propagated into the Kalman filter through the measurement-noise covariance matrix R, whose diagonal entries were set from the sensor-specific RMSE values so that each observation was weighted according to its documented error level. Process-noise covariance Q was tuned against the prototype data to ensure the innovation sequence behaved as a zero-mean sequence with autocorrelation consistent with the Kalman assumptions. Model-parameter uncertainty in hydraulic conductivity, saturated water content, cohesion, and friction angle was represented by bounded uniform distributions informed by the triaxial and permeability laboratory tests on the tailings analog, and these distributions were sampled in the Monte Carlo propagation to produce 5th and 95th percentile envelopes for both pond level and factor of safety. The resulting uncertainty bands were then carried into the decision module, where the risk score was evaluated not only at the mean factor of safety but also at its lower confidence bound, so that an action recommended under a mean-value assessment would be escalated earlier if the lower-bound estimate had already crossed the action threshold. This structure prevents the decision rule from issuing over-confident recommendations when measurement noise or parameter variability is large, and it reduces the risk of missed early actions when the mean state appears acceptable but its uncertainty envelope crosses the safety limit.

These methods formed a clear workflow that connects monitoring, simulation, and decision support. The physical prototype supplied controlled data. The DT supplied real-time state estimates and scenario tests. The decision module turned outputs into clear actions. The design stayed in line with the study goals. It also gave a method that others can copy for managing tailings dams.

4. Results and Discussions

4.1 Instrumentation performance and data coherence

Calibration accuracy and short-term drift were quantified for each sensor type, and Table 1 reports the resulting error metrics across all runs.

The error levels in Table 1 stayed below 2 percent of full scale for all sensors. Pore pressure errors stayed under 1 kPa. This level supported stable estimation of effective stress during transient loading. Pond level errors stayed below 2 mm. Crest settlement errors stayed below 0.2 mm. Drift stayed small over 24 h. These results show that measurement noise and bias stayed low compared to the observed changes during scenarios.

The study ran a time-aligned analysis of pond level, pore pressure, and crest settlement for the high-rainfall scenario. This analysis checked data coherence. Figure 1 presents this analysis across three panels. Figure 1a shows the pond level response over time during the rainfall pulse and the subsequent controlled release. Figure 1b shows the mid-slope

Table 1. Calibration accuracy and drift metrics for instrumentation.

Sensor	Range	Mean absolute error	RMSE	24 h drift
Pore pressure piezometer	0 to 80 kPa	0.7 kPa	0.9 kPa	0.5 kPa
Pond level transducer	0 to 0.50 m	1.1 mm	1.5 mm	0.8 mm
Crest settlement transducer	0 to 20 mm	0.10 mm	0.13 mm	0.06 mm
Inclinometer	±5.0 mm/m	0.04 mm/m	0.06 mm/m	0.03 mm/m
Rainfall gauge	0 to 120 mm/h	0.5 mm/h	0.7 mm/h	0.3 mm/h

pore pressure response during the same event. Figure 1c shows the crest settlement response over the event window.

The trajectories in Figure 1 were coherent in timing and magnitude. Pond level increased from 0.18 m to 0.33 m over 90 min and decreased to 0.24 m

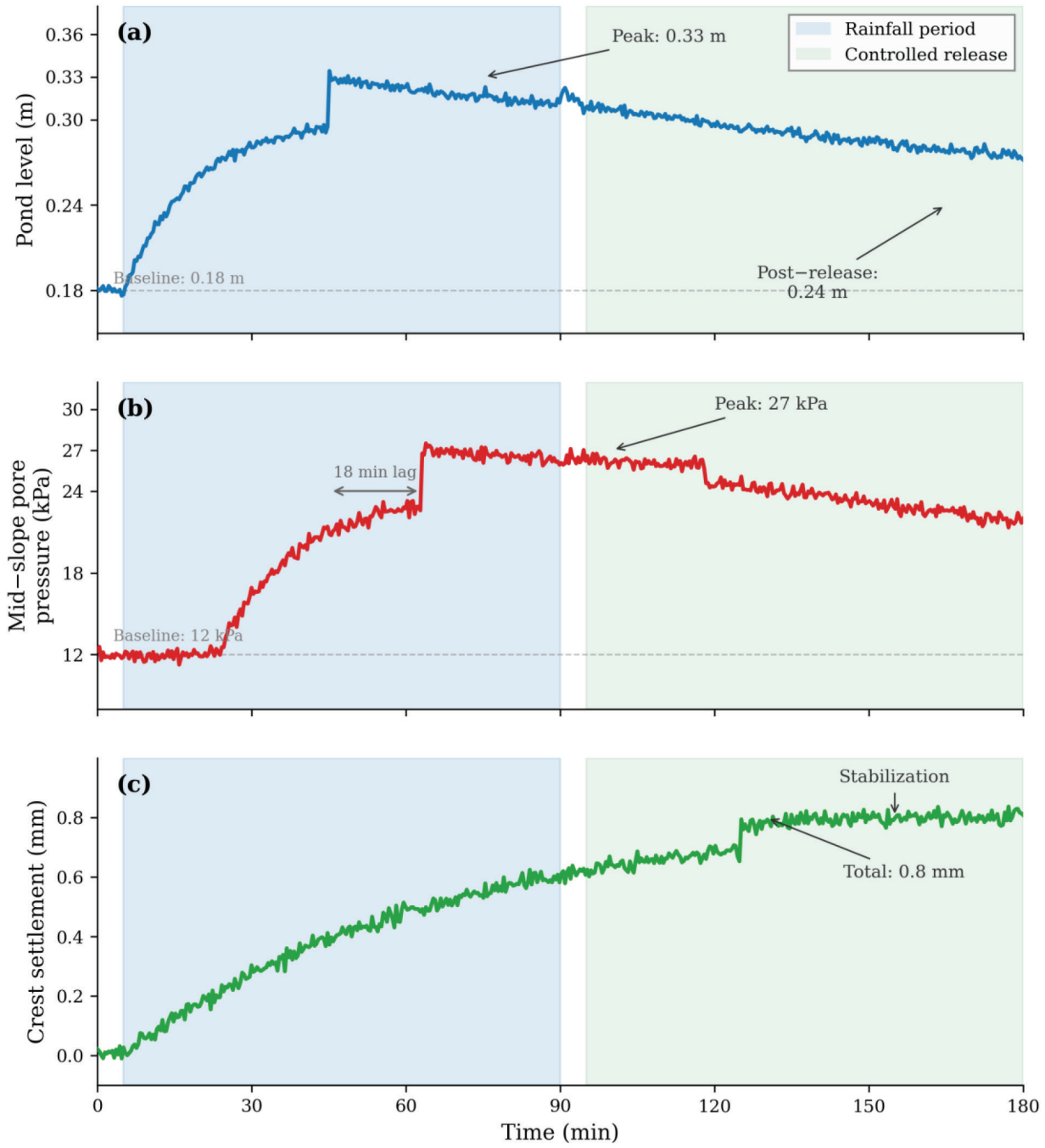

Figure 1. Time-aligned sensor responses during the high-rainfall scenario. Panel a shows pond level versus time. Panel b shows mid-slope pore pressure versus time. Panel c shows crest settlement versus time.

after controlled release. Pore pressure rose from 12 kPa to 27 kPa with an average lag of 18 min relative to pond level, which matched the expected hydraulic diffusion time in the tailings analog. Crest settlement increased by 0.8 mm over the event and stabilized after the pond level reduction. This pattern indicates that the sensor network captured the coupled hydraulic and mechanical response without evidence of spurious timing offsets.

4.2 Digital twin state estimation performance

State estimation performance was evaluated by comparing DT predictions with observed measurements in a representative rainfall scenario. Figure 2 presents this analysis across four panels. Figure 2a shows observed and predicted pond level. Figure 2b shows observed and predicted pore pressure at the mid-slope sensor. Figure 2c shows the distribution of residuals for pond level and pore pressure across the event. Figure 2d shows the autocorrelation of the innovation sequence for the same variables.

The trajectories in Figure 2a and Figure 2b tracked the observed data closely over the full event window. Residuals in Figure 2c were centered near zero, with 95 percent of pond level residuals within ±3.5 mm and 95 percent of pore pressure residuals within ±2.2 kPa. The innovation autocorrelation in Figure 2d fell below 0.2 after two lags, which indicates that the filter removed most serial dependence in measurement noise. These patterns support stable state estimation under dynamic loading.

Error metrics across all scenarios were quantified to assess general performance, and Table 2 reports the aggregated results.

Table 2 shows that error levels stayed low during the scenarios. Pond level errors didn't go above 3 mm. This value is small compared to the 0.15 m to 0.17 m changes seen during the events. Pore pressure errors stayed below 2 kPa. This is minor compared to the 15 kPa range of the event responses. These results show that the state estimation was precise. It was good enough to support decision thresholds based on pond level and factor of safety.

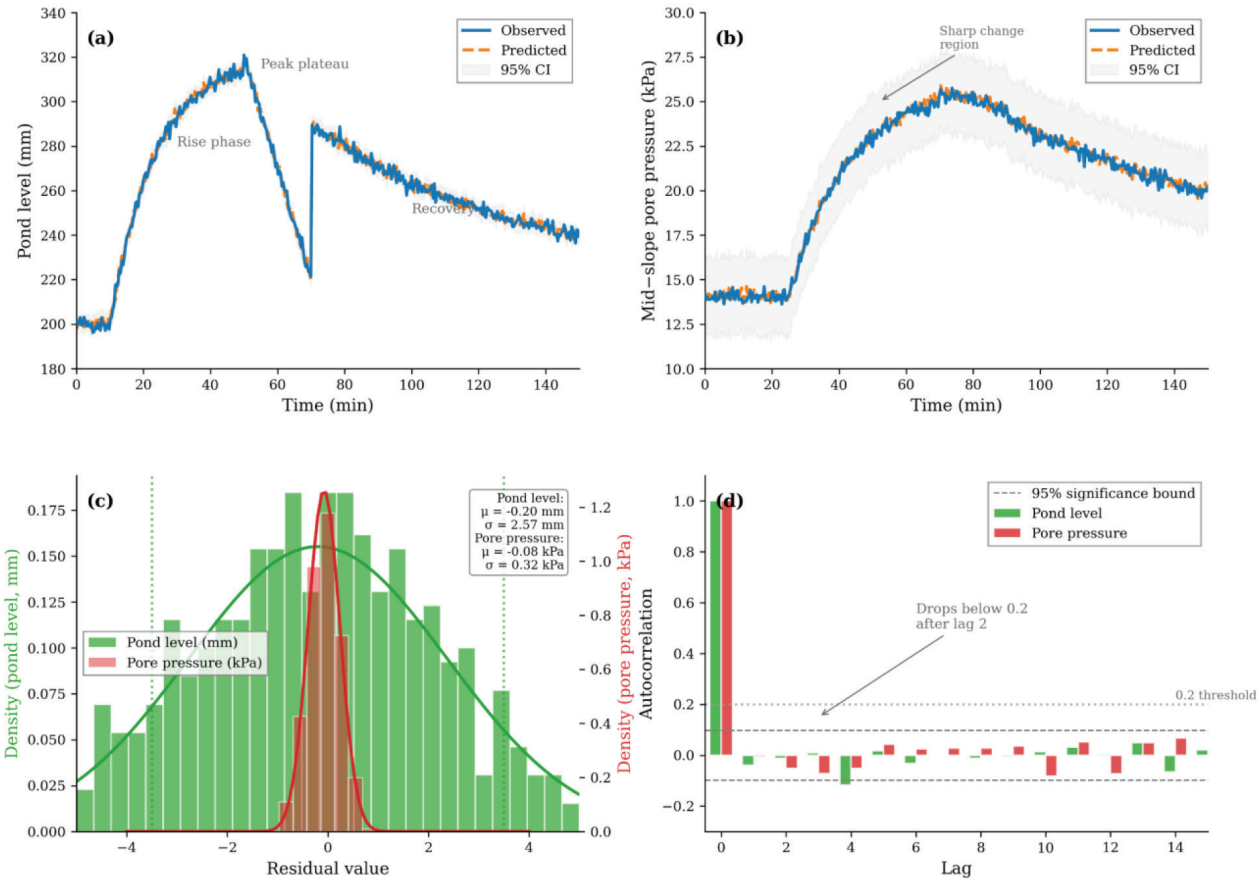

Figure 2. DT state estimation performance in a representative scenario. Panel a shows observed and predicted pond level. Panel b shows observed and predicted mid-slope pore pressure. Panel c shows residual distributions for pond level and pore pressure. Panel d shows innovation autocorrelation for both variables.

Table 2. Across-scenario DT prediction errors for key measurements.

Variable	RMSE (mean ± standard deviation)	Mean absolute error (mean ± standard deviation)	Bias (mean ± standard deviation)
Pond level	2.6 ± 0.5 mm	2.0 ± 0.4 mm	0.3 ± 0.2 mm
Pore pressure	1.9 ± 0.4 kPa	1.4 ± 0.3 kPa	0.2 ± 0.1 kPa
Crest settlement	0.18 ± 0.05 mm	0.13 ± 0.04 mm	0.02 ± 0.01 mm
Inclinometer	0.07 ± 0.02 mm/m	0.05 ± 0.02 mm/m	0.01 ± 0.01 mm/m
Rainfall rate	0.8 ± 0.2 mm/h	0.6 ± 0.2 mm/h	0.1 ± 0.1 mm/h

4.3 Hydro-mechanical response and stability outcomes

The study examined the hydro-mechanical response through phreatic surface changes, pore pressure fields, and safety margin dynamics. Figure 3 presents this analysis in four panels. Figure 3a shows phreatic surface profiles at baseline, peak rainfall, and after release. Figure 3b shows the pore pressure contour at peak rainfall. Figure 3c shows the factor of safety time series for routine, rainfall, and rapid-load scenarios. Figure 3d shows the relationship between pond level and factor of safety for those same runs.

Phreatic surfaces in Figure 3a rose by 0.14 m during peak rainfall. They returned to within 0.03 m of the baseline after release. This indicates a reversible hydraulic response during a controlled drawdown. The pore pressure contour in Figure 3b shows a high-pressure zone near the upstream face. Gradients became steeper toward the mid-slope sensor line.

The factor of safety in Figure 3c dropped from 1.62 to 1.28 during intense rainfall. Routine operation stayed above 1.55. The rapid-load scenario caused the fastest decline. The minimum occurred within 15 min of loading. Figure 3d shows a nearly linear decline in the factor of safety as the pond level

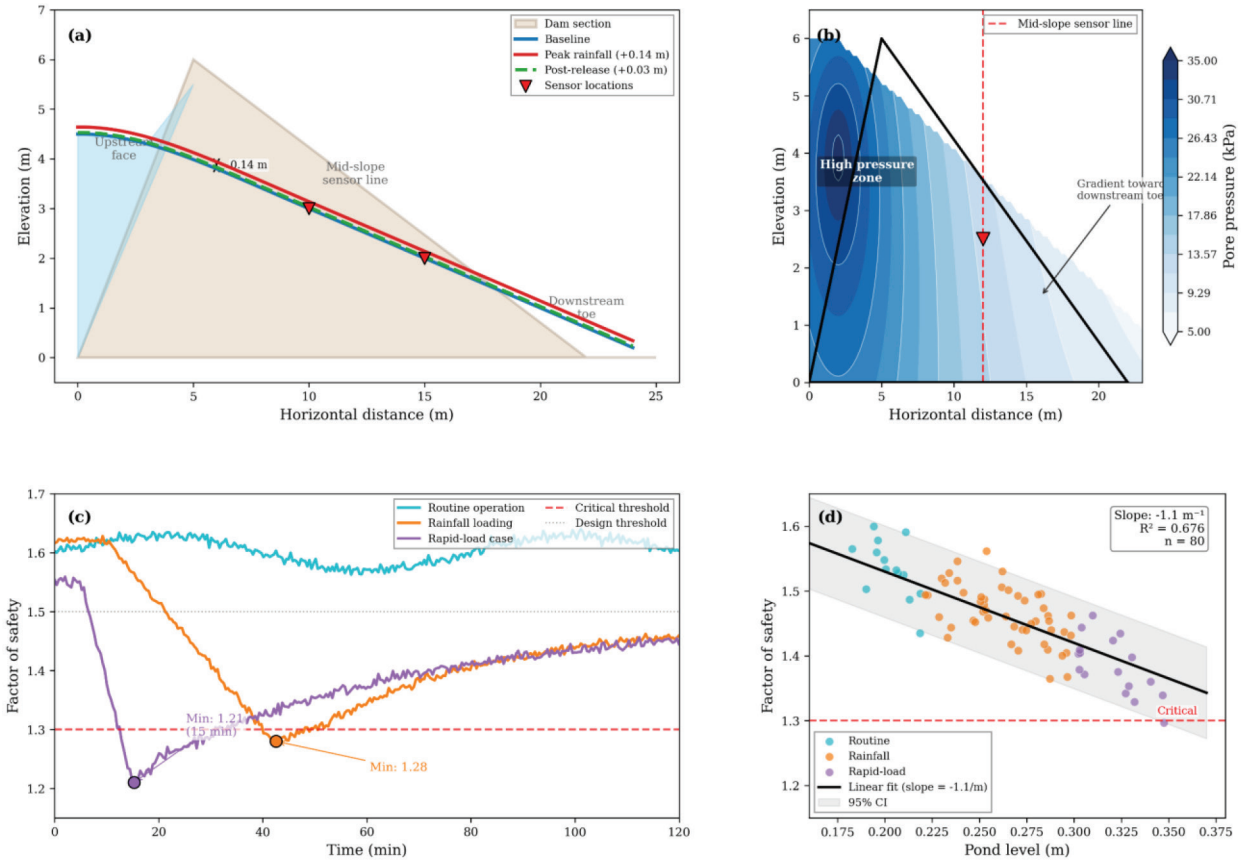

Figure 3. Hydro-mechanical response and stability trends. Panel a shows phreatic surface profiles at three times. Panel b shows a pore pressure contour at peak rainfall. Panel c shows factor of safety time series for three scenario types. Panel d shows factor of safety versus pond level.

rose. The average slope was -1.1 per meter across the scenarios. This shows that water balance control had a strong influence on stability in the prototype. Table 3 reports the minimum safety margins and their timing for each scenario.

The values in Table 3 show that rainfall produced the lowest safety margins among hydraulic scenarios, while the rapid-load case produced the fastest decline. The difference between routine and rainfall minima was 0.28, which reflects a substantial reduction in available safety margin during intense rainfall. The mid-slope pore pressures at minimum safety margin were higher in the rainfall case than in the rapid-load case, which indicates that hydraulic loading dominated that response while rapid loading emphasized transient stress conditions.

4.4 Scenario water balance and operational response

Water balance dynamics were evaluated across rainfall intensities to characterize operational exposure. Figure 4 presents this analysis across three panels. Figure 4a shows pond level trajectories for low, medium, and high rainfall intensity scenarios. Figure 4b shows discharge rates over time for the same scenarios. Figure 4c shows seepage flux at the downstream drainage layer.

Pond level responses in Figure 4a separated clearly by rainfall intensity. High intensity rainfall produced a peak pond level of about 0.34 m and a prolonged period above the target operating level. Medium intensity produced a peak near 0.30 m, while low intensity remained below 0.28 m. Discharge rates in Figure 4b increased with rainfall intensity and were activated earlier under high intensity conditions, with peak discharge occurring 30 to 40 min after the rainfall peak. Seepage flux in Figure 4c increased from 0.6 L/min at baseline to 1.8 L/min at peak rainfall, which indicates a strong hydraulic response in the drainage layer. Operational exceedance metrics were quantified for each rainfall intensity, and Table 4 reports these results.

The values in Table 4 show that the time spent above the limit rose sharply as rainfall got heavier. The low-intensity scenario stayed below the target level. This meant those runs didn't need any corrective actions. High-intensity rainfall stayed above the target for nearly an hour. This required the largest water releases and caused the biggest temporary drop in the deposition rate. These results show that rainfall intensity is the main cause of operational problems in the prototype.

4.5 Decision support outputs and action sequencing

The study looked at decision support outputs to see how the system chose and timed its actions. Figure 5 shows this analysis in four parts. Figure 5a displays the cost levels over time for the high-rainfall scenario. Figure 5b shows the mapped failure probability as it relates to the factor of safety. Figure 5c shows the timeline for when the pond release and deposition changes happened. Figure 5d shows the changes in pond level and factor of safety after those actions occurred.

In Figure 5a, the safety part of the cost dominated during the heaviest rain. The deposition part dominated during the recovery phase. Figure 5b shows that the mapped failure probability rose quickly once the factor of safety dropped below 1.35. This matches the action threshold that the decision logic used. Figure 5c shows that the system triggered the first release 24 min before the safety factor reached its lowest point. A short drop in the deposition rate followed. Figure 5d shows that the pond level fell by 0.06 m within 45 min after the release. The factor of safety also recovered from 1.29 to 1.41 during that same time. These patterns show that the decision support module linked water changes to fast actions.

4.6 Validation, benchmarking, and ablation

Comparative benchmarking against baseline approaches was conducted to assess operational bene-

Table 3. Minimum factor of safety and timing by scenario type.

Scenario type	Minimum factor of safety (mean ± standard deviation)	Time to minimum (min)	Pore pressure at mid-slope at minimum (kPa)
Routine operation	1.58 ± 0.04	85 ± 12	16 ± 1.5
Rainfall loading	1.30 ± 0.05	42 ± 8	27 ± 2.0
Rapid-load case	1.21 ± 0.06	12 ± 3	22 ± 1.8

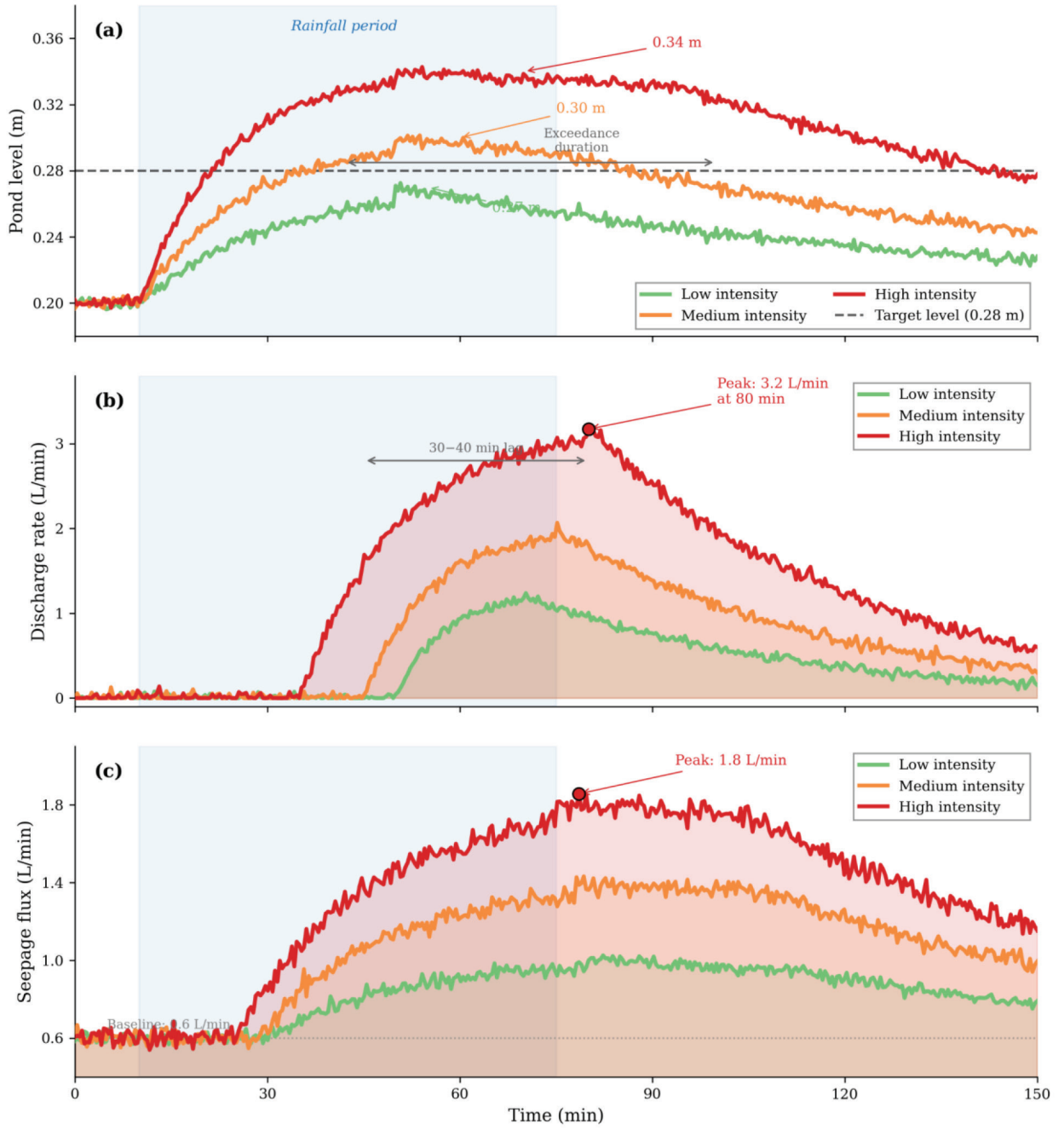

Figure 4. Water balance dynamics across rainfall intensities. Panel a shows pond level trajectories for low, medium, and high rainfall. Panel b shows discharge rates over time. Panel c shows seepage flux at the drainage layer.

Table 4. Pond level exceedance and discharge metrics by rainfall intensity.

Rainfall intensity	Peak pond level (m)	Time above target level 0.28 m (min)	Cumulative discharge (L)	Net deposition reduction (%)
Low	0.27 ± 0.01	0 ± 0	18 ± 4	2.1 ± 0.8
Medium	0.30 ± 0.01	22 ± 6	34 ± 5	4.6 ± 1.0
High	0.34 ± 0.02	58 ± 9	62 ± 8	9.8 ± 1.4

fits. Table 5 reports mean ± standard deviation values and percentage improvements for the proposed DT relative to the rule-based threshold baseline.

The metrics in Table 5 indicate that the proposed DT reduced response time and peak pond level while increasing the minimum factor of safety relative to the rule-based baseline. Paired t-tests across scenarios showed a response time reduction of 13 min

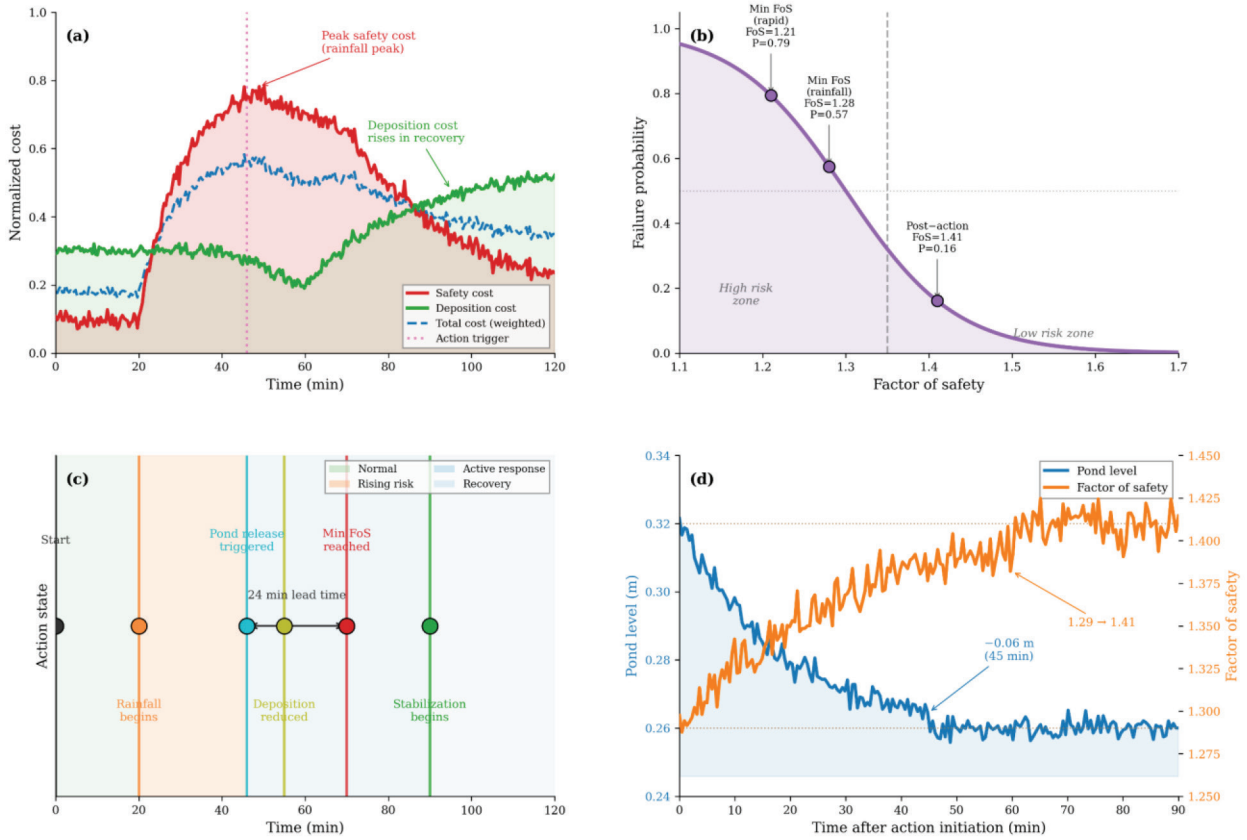

Figure 5. Decision support outputs and operational actions. Panel a shows normalized cost components over time. Panel b shows the mapped failure probability versus factor of safety. Panel c shows the action timeline for pond release and deposition adjustment. Panel d shows pond level and factor of safety responses following actions.

Table 5. Benchmarking of operational performance across control strategies with mean ± standard deviation and improvement relative to the rule-based baseline.

Metric	Periodic inspection baseline	Rule-based threshold baseline	Static LEM baseline	Proposed DT	Improvement vs rule-based baseline (%)
Response time to first action (min)	52 ± 8	34 ± 7	41 ± 6	21 ± 5	38.2
Minimum factor of safety	1.24 ± 0.06	1.28 ± 0.05	1.30 ± 0.05	1.36 ± 0.04	6.3
Peak pond level (m)	0.35 ± 0.02	0.33 ± 0.02	0.34 ± 0.02	0.29 ± 0.01	12.1
Deposition deviation (%)	3.1 ± 1.2	6.4 ± 1.6	2.9 ± 1.0	3.2 ± 1.1	50.0
Alerts per scenario	0.6 ± 0.5	1.8 ± 0.7	0.9 ± 0.6	1.1 ± 0.5	38.9

with $p < 0.001$ and Cohen's d of 1.4. The increase in minimum factor of safety was 0.08 with $p = 0.004$ and Cohen's d of 1.1. Peak pond level reduction was 0.04 m with $p < 0.001$ and Cohen's d of 1.6. Deposition deviation for the proposed DT did not differ significantly from the static LEM baseline, with $p = 0.18$ and Cohen's d of 0.3, which indicates that the operational efficiency gain was limited for that metric. Alert counts were lower than the rule-based baseline but higher than periodic inspection, which indicates a trade-off between early action and alarm frequency.

Ablation analysis assessed the contribution of core components within the DT framework. Figure 6 presents this analysis across four panels. Figure 6a shows the effect of removing the Kalman filter on pond level and pore pressure prediction errors. Figure 6b shows the effect of removing seepage coupling on minimum factor of safety error. Figure 6c shows response time for full DT versus the rule-based decision module without optimization. Figure 6d shows false alarm counts for full DT versus a binary threshold decision without risk mapping.

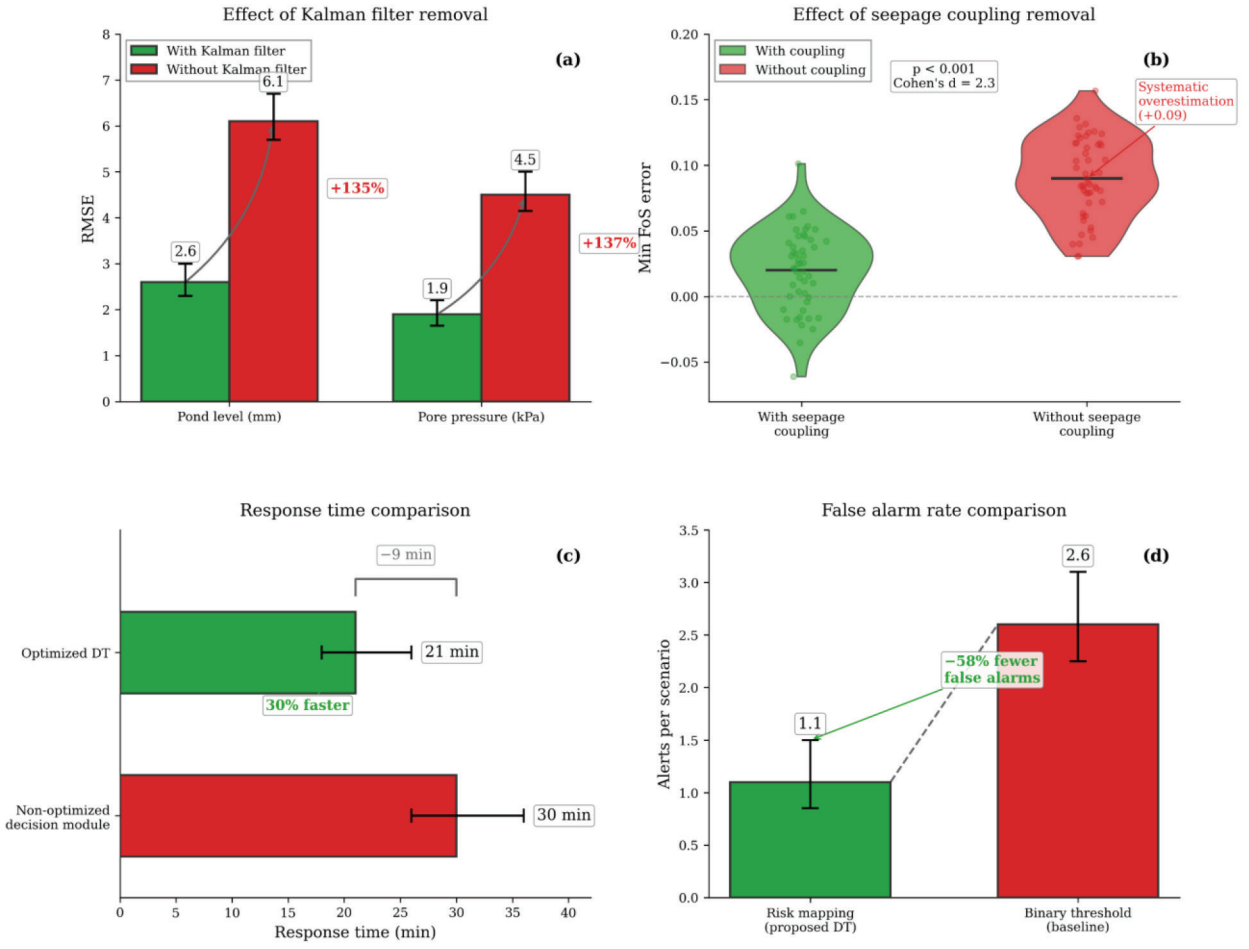

Figure 6. Ablation results for DT components. Panel a shows prediction errors with and without the Kalman filter. Panel b shows minimum factor of safety error when seepage coupling is removed. Panel c shows response time with and without optimization. Panel d shows false alarm counts with and without risk mapping.

Figure 6a shows the ablation results. Removing the Kalman filter increased pond level RMSE from 2.6 mm to 6.1 mm. It also raised pore pressure RMSE from 1.9 kPa to 4.5 kPa. Figure 6b shows that removing seepage coupling led to a consistent overestimation of the minimum factor of safety. The results were 0.09 higher on average, which made safety thresholds less reliable. Figure 6c shows that removing optimization increased response time from 21 min to 30 min. This change didn't leave as much time for intervention. Figure 6d shows that removing risk mapping increased false alarms from 1.1 to 2.6 per scenario. Probabilistic risk scaling helped stop unnecessary actions. These results confirm that each part of the system offered a specific benefit.

4.7 Uncertainty and sensitivity outcomes

Uncertainty analysis measured the changes in key outcomes across different random trials. Figure 7 presents this analysis in three panels. Figure 7a shows the spread of the minimum factor of safety for the high-rainfall scenario. Figure 7b shows the spread of the peak pond level for the same scenario. Figure 7c shows the link between hydraulic conductivity and the minimum factor of safety.

The data in Figure 7a shows an average minimum factor of safety of 1.32. The 5th percentile was 1.21 and the 95th percentile was 1.43. Figure 7b shows an average peak pond level of 0.32 m. The 5th percentile was 0.29 m and the 95th percentile was 0.35 m. Figure 7c shows a negative connection between hydraulic conductivity and the minimum factor of safety. The correlation was -0.62. This indicates that higher conductivity increased the pore pressure response during rainfall. This response reduced stability margins.

The study calculated sensitivity coefficients to measure how much certain parameters affected the model. Table 6 reports standardized regression coefficients for three outputs.

The coefficients in Table 6 show that hydraulic conductivity and rainfall intensity dominated minimum factor of safety and peak pond level, while

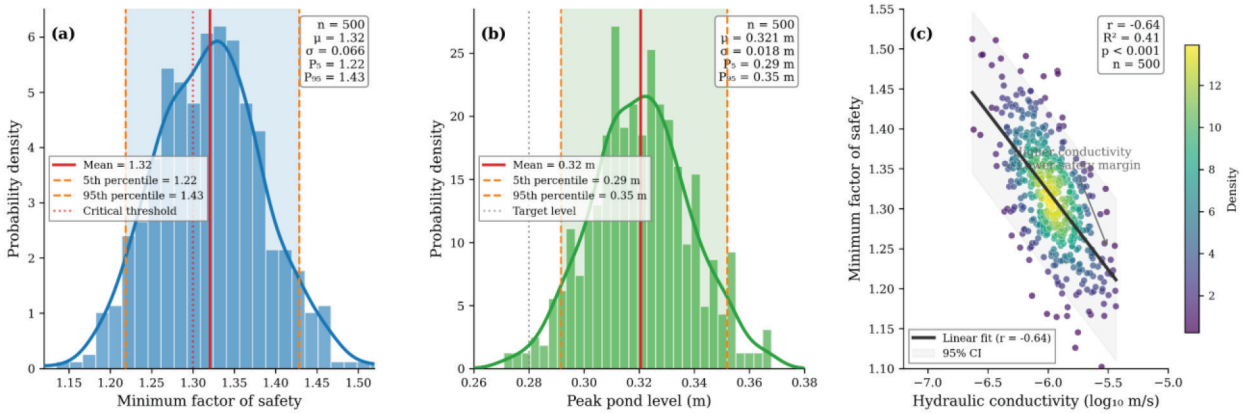

Figure 7. Uncertainty analysis outcomes. Panel a shows the distribution of minimum factor of safety. Panel b shows the distribution of peak pond level. Panel c shows the relationship between hydraulic conductivity and minimum factor of safety.

Table 6. Standardized regression coefficients linking parameters to key outcomes.

Parameter	Minimum factor of safety	Peak pond level	Response time to action
Hydraulic conductivity	-0.48	0.36	0.22
Cohesion	0.31	-0.05	-0.08
Friction angle	0.42	-0.07	-0.10
Rainfall intensity	-0.37	0.51	0.34
Deposition rate	-0.21	0.19	0.27

deposition rate had a stronger effect on response time. Cohesion and friction angle had strong positive effects on safety margin but weak effects on pond level. These results indicate that hydraulic parameters drove the most variable outcomes under rainfall loading, while mechanical parameters shaped the absolute safety margin.

The results show that the DT shifted operations from delayed response to earlier, targeted action. The reduction in response time and the recovery of FoS after release indicate that data assimilation and scenario testing shaped decisions rather than only confirming conditions. The low state estimation errors for pond level and pore pressure relative to event amplitudes show that the decision logic acted on stable inputs, which supports the reliability of the action thresholds.

The findings align with monitoring studies that link hydraulic loading to deformation and pore pressure signals and support early warning [46], [47]. The results also extend risk assessment work by adding a closed loop decision layer to time dependent risk management [48]. DT frameworks in civil infrastructure emphasize synchronization and scenario testing, and the observed decision gains are consistent with that emphasis [49], [50]. The divergence from many monitoring studies lies in the prescriptive step. Those studies often stop at detection or visualization, whereas the present results show how the same signals can be converted into operational actions.

5. Conclusions

This study concludes that the DT framework delivers earlier and more consistent operational decisions while preserving safety margins under stress. The response time to first action dropped from 34 to 21 minutes versus the rule-based baseline, with $p < 0.001$ and Cohen's d of 1.4, which shows a clear shift in decision timing. The minimum FoS increased from 1.28 to 1.36 with $p = 0.004$ and $d = 1.1$, and the peak pond level fell from 0.33 m to 0.29 m with $p < 0.001$ and $d = 1.6$, which links earlier releases to safer hydraulic states without large production penalties.

The core methodological contribution is the closed loop linkage between monitoring, hydro-mechanical simulation, and prescriptive action. State estimation errors were small relative to event changes, with pond level RMSE of 2.6 mm and pore pressure RMSE of 1.9 kPa, which supports the reliability of the decision rules. The negative relation between pond level and FoS had a slope near −1.1 per meter, and scenario contrasts showed that rainfall loading reduced FoS to

about 1.30 while routine operation stayed near 1.58, which confirms that water balance control is the main operational lever in the tested conditions.

The study has limits that affect generalization. The scenario set is narrow, material properties are uniform, and decision weights are fixed, which may bias performance toward the tested conditions. Sensor placement also reflects a single geometry and may not capture all failure modes. Future work should broaden the scenario library, calibrate parameters with long term records, and test adaptive thresholds that respond to evolving conditions.

The 1:60 geometric scale of the physical prototype was selected for controlled repeatability, but it introduces well-known distortions that must be acknowledged when the decision logic is transferred to full-scale tailings storage facilities. Under a 1g bench scale the effective-stress levels are far below prototype values, which shifts the operating branch of the soil-water retention curve and the stress-dependent hydraulic conductivity of the tailings analog. Free-surface hydraulics on the pond follow a Froude-type similarity, whereas seepage through the embankment body is Reynolds- and capillarity-sensitive; these two regimes cannot be satisfied simultaneously under a single geometric scaling, and the resulting time-scale mismatch means that pore-pressure diffusion in the scaled model does not reproduce prototype consolidation times without explicit time-scale correction. The drainage-layer response and the phreatic-surface transients observed in the laboratory therefore represent a dimensionally consistent qualitative analogue of field behavior rather than a one-to-one quantitative replica. The practical implication is that the absolute numerical thresholds reported in this study, such as the 1.35 action value of the factor of safety, should be recalibrated against site-specific material tests and historical instrumentation records before they are applied to a real facility. What is expected to transfer more robustly is the architecture of the decision loop itself, namely the coupling between Kalman-filtered state estimation, hydro-mechanical simulation, and the weighted cost function, because that architecture is independent of the geometric scale and only depends on the quality of the calibration data feeding it.

The analog used a controlled mixture of silica sand, kaolinite, and silt chosen to represent a typical metal-mine tailings envelope, and its mixture ratio was held constant across all runs. A formal sensitivity analysis on the mixture ratio was not performed, because the objective of the prototype was to isolate the behavior of the closed-loop decision logic rather than to explore the full field-scale parameter space. This is a recognized limitation. Real tailings deposits are typically non-homogeneous, multi-modal, and anisotropic in both grain-size distribution and compaction state, with beach-to-pond segregation, interbedded fines, and spatial variability in hydraulic conductivity that the present analog does not reproduce. Consequently, the physical-to-numerical model divergence reported here is an optimistic lower bound on the divergence that would be observed in a real facility, and the risk-score calibration of the decision module would need to be widened to accommodate the higher parameter variability of site tailings. This limitation motivates future work on stochastic heterogeneous analogs and on Bayesian updating of the DT against in-service instrumentation records.

The fixed-weight formulation used here is an engineering simplification. In operational practice, the safety, pond-level, and deposition-deviation weights should be treated as governance parameters that are dynamically reconciled to the site-specific risk appetite and to the prevailing loading regime. In high-seismicity regions, the safety weight should dominate so that any factor-of-safety reduction, however small, is penalized aggressively and the rapid-load branch of the decision logic is activated earlier. In high-rainfall or monsoon-exposed regions, the pond-level weight should be raised during the wet season so that early discharge actions are taken before pond storage is exhausted. In cold-climate or reclamation-phase facilities with diminished production pressure, the deposition-deviation weight can be relaxed to allow more aggressive production pauses in response to emerging risk signals. A promising extension of the present framework is to couple these weights to an updating module that ingests a site-specific hazard model, seasonal climate forecasts, and the operator's declared risk tolerance, so that the decision surface is reshaped automatically as external conditions change rather than requiring a manual re-tuning.

Future research should integrate satellite InSAR with in situ sensing, test the framework across dam types, and evaluate alarm fatigue under continuous operations. It should also compare cost functions that include environmental loss alongside operational metrics to examine how decision trade-offs change.

Disclosure

During the preparation of this work, the author used ChatGPT to improve readability and language. After using this tool, the author reviewed and edited the content as needed and takes full responsibility for the content of the publication.

Funding

This research did not receive any specific grant from funding agencies in the public, commercial, or not-for-profit sectors.

References

[1] F. F. Garcia, C. F. Camilo Cotrim, S. S. Caramori, and E. A. Silva, "Mine tailings dams' failures: Serious environmental impacts, remote solutions," Environ. Dev. Sustain., vol. 27, pp. 18179–18201, 2025, doi: 10.1007/s10668-024-04628-z.

[2] S.-Q. Lin, G.-J. Wang, W.-L. Liu, B. Zhao, Y.-M. Shen, M.-L. Wang, and X.-S. Li, "Regional distribution and causes of global mine tailings dam failures," Metals, vol. 12, no. 6, p. 905, 2022, doi: 10.3390/met12060905.

[3] W. Xiong, C. S. Cai, R. Zhang, H. Shi, and C. Xu, "Review of hydraulic bridge failures: Historical statistic analysis, failure modes, and prediction methods," J. Bridge Eng., vol. 28, no. 4, 2023, doi: 10.1061/JBENF2.BEENG-5763.

[4] H. Yu, I. Zahidi, C. M. Fai, D. Liang, and D. Ø. Madsen, "Tailings dam failures: A critical evaluation of current policies and practices," Results Eng., vol. 25, p. 103973, 2025, 10.1016/j.rineng.2025.103973.

[5] R. N. Guimarães, V. R. Moreira, J. R. Cruz, A. P. Saliba, and M. C. Amaral, "History of tailings dam failure: Impacts on access to safe water and influence on the legislative framework," Sci. Total Environ., vol. 852, p. 158536, 2022, doi: 10.1016/j.scitotenv.2022.158536.

[6] M. Wu, Y. Ye, N. Hu, Q. Wang, and W. Tan, "Scientometric analysis on the review research evolution of tailings dam failure disasters," Environ. Sci. Pollut. Res., vol. 30, no. 6, pp. 13945–13959, 2023, doi: 10.1007/s11356-022-24937-y.

[7] C. Su, N. M. Rana, S. G. Evans, B. Wang, and S. Zhang, "Tailings storage facilities in China: Historical failure incidents, existing status, and database-driven quantitative risk assessment," Int. J. Disaster Risk Reduct., vol. 114, p. 104973, 2024, doi: 10.1016/j.ijdrr.2024.104973.

[8] K. A. Hudson-Edwards et al., "Tailings storage facilities, failures and disaster risk," Nat. Rev. Earth Environ., vol. 5, no. 9, pp. 612–630, 2024, doi: 10.1038/s43017-024-00576-4.

[9] S. Ouellet, J. Dettmer, T. D. Mikesell, M. Lato, and M. Karrenbach, "Tailings dam performance monitoring by combining coda wave interferometry with distributed acoustic sensing," J. Geotech. Geoenviron. Eng., vol. 151, no. 6, p. 04025035, 2025, doi: 10.1061/JGGEFK.GTENG-13066.

[10] C. Crous and L. Marais, "Transparency of reporting on tailings storage facilities by the six largest members of the International Council on Mining and Metals," Resour. Policy, vol. 111, p. 105784, 2025, doi: 10.1016/j.resourpol.2025.105784.

[11] R. L. Rose, S. R. Mugi, and J. H. Saleh, "Accident investigation and lessons not learned: AcciMap analysis of successive tailings dam collapses in Brazil," Reliab. Eng. Syst. Saf., vol. 236, p. 109308, 2023, doi: 10.1016/j.ress.2023.109308.

[12] C. A. D. Fraga Filho and R. Aleixo, "Major recent failures in Brazilian mine waste containment facilities, current cases of maximum emergency level and imminent risk of rupture, and a brief sustainability analysis," Environ. Sci. Pollut. Res., vol. 31, pp. 56399–56427, 2024, doi: 10.1007/s11356-024-34864-9.

[13] R. S. Massignan, J. Siqueira-Gay, and L. E. Sánchez, "Setting a comprehensive bow-tie framework for disaster risk analysis of mine tailings storage facilities," Risk Anal., vol. 45, no. 12, pp. 4604–4618, 2025, doi: 10.1111/risa.70137.

[14] C. Chen, Y. Zhao, and B. Ma, "Three-dimensional risk matrix for risk assessment of tailings storage facility failure: Theory and a case study," Geotech. Geol. Eng., vol. 42, pp. 1811–1833, 2024, doi: 10.1007/s10706-023-02647-7.

[15] J. Atta and A. K. Bera, "Slope safety factor (FoS): Decoding definitions through analogical discussion," Nat. Hazards, vol. 121, no. 17, pp. 19591–19629, 2025, doi: 10.1007/s11069-025-07606-4.

[16] M. Zare, F. Nasategay, J. A. Gomez, A. Moayedi Far, and J. Sattarvand, "A review of tailings dam safety monitoring guidelines and systems," Minerals, vol. 14, no. 6, p. 551, 2024, doi: 10.3390/min14060551.

[17] W. Nie, M. Luo, Y. Wang, and R. Li, "3D visualization monitoring and early warning system of a tailings dam—Gold copper mine tailings dam in Zijinshan, Fujian, China," Front. Earth Sci., vol. 10, p. 800924, 2022, doi: 10.3389/feart.2022.800924.

[18] W. Nie, J. Chen, D. Song, L. Dong, X. Liu, and E. Wang, "Three-dimensional intelligent monitoring and early warning technology for tailings ponds based on spatiotemporal fusion of multisource big data," Environ. Monit. Assess., vol. 196, no. 11, p. 1081, 2024.

[19] C. Cacciuttolo, V. Guzmán, P. Catriñir, and E. Atencio, "Sensor technologies for safety monitoring in mine tailings storage facilities: Solutions in the Industry 4.0 era," Minerals, vol. 14, no. 5, p. 446, 2024, doi: 10.3390/min14050446.

[20] M. Bayaraa, B. Sheil, and C. Rossi, "InSAR and numerical modelling for tailings dam monitoring – the Cadia failure case study," Geotechnique, vol. 74, no. 10, pp. 985–1003, 2024, doi: 10.1680/jgeot.21.00399.

[21] T. Jia, "Optimizing construction project plan management using parameter-adaptive improved genetic algorithm," Teh. Vjesn., vol. 32, no. 1, pp. 98–106, 2025, doi: 10.17559/TV-20240720001868.

[22] L. Lu, M. Li, and L. Chao, "Integration of InSAR and numerical modelling to assess tailings pond slope deformation affected by reservoir water," Sci. Rep., vol. 15, p. 43304, 2025, doi: 10.1038/s41598-025-27314-0.

[23] T. V. Emani, "Enhancing construction site monitoring and cost efficiency through drone technology," J. Eng. Manag. Ind. Technol. (JEMIT), vol. 4, no. 2, pp. 163–170, 2026, doi: 10.61552/JEMIT.2026.02.005.

[24] S. Das, A. Priyadarshana, and S. Grebby, "Monitoring the risk of a tailings dam collapse through spectral analysis of satellite InSAR time-series data," Stoch. Environ. Res. Risk Assess., vol. 38, pp. 2911–2926, 2024, doi: 10.1007/s00477-024-02713-3.

[25] A. H.-M. Ng, Z. Liu, Z. Du, H. Huang, H. Wang, and L. Ge, "A novel framework for combining polarimetric Sentinel-1 InSAR time series in subsidence monitoring – A case study of Sydney," Remote Sens. Environ., vol. 295, p. 113694, 2023, doi: 10.1016/j.rse.2023.113694.

[26] E. Giorgini, F. Orellana, C. Arratia, L. Tavasci, G. Montalva, M. Moreno, and S. Gandolfi, "InSAR monitoring using Persistent Scatterer Interferometry (PSI) and Small Baseline Subset (SBAS) techniques for ground deformation measurement in metropolitan area of Concepción, Chile," Remote Sens., vol. 15, no. 24, p. 5700, 2023, doi: 10.3390/rs15245700.

[27] P. Wang, H. Yang, and J. Jie, "Pumped storage power plant dam deformation monitoring and early warning system based on multi-source heterogeneous data," Aust. J. Electr. Electron. Eng., pp. 1–19, 2025, doi: 10.1080/1448837X.2025.2560692.

[28] F. Samadzadegan, A. Toosi, and F. Dadrass Javan, "A critical review on multi-sensor and multi-platform remote sensing data fusion approaches: Current status and prospects," Int. J. Remote Sens., vol. 46, no. 3, pp. 1327–1402, 2025, doi: 10.1080/01431161.2024.2429784.

[29] N. Kazanskiy, R. Khabibullin, A. Nikonorov, and S. Khonina, "A comprehensive review of remote sensing and artificial intelligence integration: Advances, applications, and challenges," Sensors, vol. 25, no. 19, p. 5965, 2025, doi: 10.3390/s25195965.

[30] X. Yang, et al., "Advances in UAV remote sensing for monitoring crop water and nutrient status: Modeling methods, influencing factors, and challenges," Plants, vol. 14, no. 16, p. 2544, 2025, doi: 10.3390/plants14162544.

[31] S. Asadzadeh and C. R. Souza Filho, "Numerical modeling of land surface temperature over complex geologic terrains: A remote sensing approach," Remote Sens., vol. 15, no. 19, p. 4877, 2023, doi: 10.3390/rs15194877.

[32] S. N. M. Aldouri, "Digital twin-enabled Just-In-Time and Kanban implementation framework for Industry 4.0 transformation in SMEs," Int. J. Ind. Eng. Manag., vol. 16, no. 4, pp. 339–358, 2025, doi: 10.24867/IJIEM-392.

[33] O. Ojo and R. Shittu, "Design and finite element method based structural analysis of a PET bottles-to-plastic flakes recycling plant," Int. J. Ind. Eng. Manag., vol. 14, no. 1, pp. 25–40, 2023, doi: 10.24867/IJIEM-2023-1-322.

[34] M. Siahkouhi, M. Rashidi, F. Mashiri, F. Aslani, and M. S. Ayubirad, "Application of self-sensing concrete sensors for bridge monitoring – A review of recent developments, challenges, and future prospects," Measurement, vol. 245, p. 116543, 2025, doi: 10.1016/j.measurement.2024.116543.

[35] F. Emmert-Streib, "Defining a digital twin: A data science-based unification," Mach. Learn. Knowl. Extr., vol. 5, no. 3, pp. 1036–1054, 2023, doi: 10.3390/make5030054.

[36] P. G. Brarda, G. Fernandez, and N. F. Ayala, "Digital Twin, Digital Shadow or Digital Model? A systematic literature review," in Advances in Production Management Systems. Cyber-Physical-Human Production Systems: Human-AI Collaboration and Beyond, H. Mizuyama, E. Morinaga, T. Nonaka, T. Kaihara, G. von Cieminski, and D. Romero, Eds., IFIP Advances in Information and Communication Technology, vol. 766, Cham: Springer Nature Switzerland, 2026, pp. 306–319, doi: 10.1007/978-3-032-03538-7_22.

[37] R. Mohanraj and S. N. Balaji, "Digital twin technology: A comprehensive review of modeling, applications, challenges and future directions in complex system integration," Arch. Comput. Methods Eng., vol. 33, pp. 3291–3316, 2026, doi: 10.1007/s11831-025-10397-3.

[38] A. Waqar and N. Shafiq, "Impact of digital twin technology implementation on the lifecycle management of structural assets," Eng. Constr. Archit. Manag., ahead of print, 2025, doi: 10.1108/ECAM-01-2025-0011.

[39] K. Y. H. Lim, P. Zheng, and C.-H. Chen, "A state-of-the-art survey of digital twin: Techniques, engineering product lifecycle management and business innovation perspectives," J. Intell. Manuf., vol. 31, pp. 1313–1337, 2020, doi: 10.1007/s10845-019-01512-w.

[40] K. Rogage, E. Mahamedi, I. Brilakis, and others, "Beyond digital shadows: A digital twin for monitoring earthwork operation in large infrastructure projects," AI Civ. Eng., vol. 1, p. 7, 2022, doi: 10.1007/s43503-022-00009-5.

[41] M. Barzegar, S. Blanks, B.-A. Sainsbury, and W. Timms, "MEMS technology and applications in geotechnical monitoring: A review," Meas. Sci. Technol., vol. 33, no. 5, p. 052001, 2022, doi: 10.1088/1361-6501/ac4f00.

[42] A. Alrabghi, "A modelling approach for asset degradation: Advancing digital twin in maintenance," Int. J. Simul. Model., vol. 24, no. 1, pp. 76–86, 2025, doi: 10.2507/IJSIMM24-1-715.

[43] L. El Hiouile, A. Errami, and N. Azami, "Towards Mine 4.0: A proposed multi-layered architecture for real-time surveillance and anomaly detection in an open-pit phosphate mine," Mining, vol. 4, no. 3, pp. 672–686, 2024, doi: 10.3390/mining4030038.

[44] M. Wahbah, M. Chehadeh, M. Hamandi, L. Seneviratne, and Y. Zweiri, "Real-time adaptive dynamics based state estimation scheme for unmanned aircrafts," IEEE Sens. J., vol. 22, no. 14, pp. 14397–14414, 2022, doi: 10.1109/JSEN.2022.3183187.

[45] A. Baldassarre, J.-L. Dion, N. Peyret, and F. Renaud, "Digital twin with augmented state extended Kalman filters for forecasting electric power consumption of industrial production systems," Heliyon, vol. 10, no. 6, p. e27343, 2024.

[46] Y. Xu, T. Bao, S. Zhang, and others, "Innovative approach for experimental investigation and monitoring and warning of the evolutionary patterns of dam body failure in earth dams," Sci. Rep., vol. 15, p. 14367, 2025, doi: 10.1038/s41598-025-97057-5.

[47] K. Ma, Z. Yuan, Z. Gao, F. Ren, and H. Ke, "The early warning method of Dagangshan high-arch dam risk based on the time series prediction of the multivariate monitoring data," Struct. Health Monit., vol. 25, no. 2, pp. 1237–1256, 2026, doi: 10.1177/14759217241306989.

[48] D. Alves, C. F. Oliveira, S. C. Marsal, R. N. Souza, and L. P. C. Fonseca, "Monitoring and reporting dam safety operational risks based on bow tie methodology," Process Saf. Prog., vol. 42, no. S1, pp. S56–S71, 2023, doi: 10.1002/prs.12449.

[49] D. Wu, A. Zheng, W. Yu, H. Cao, Q. Ling, J. Liu, and D. Zhou, "Digital twin technology in transportation infrastructure: A comprehensive survey of current applications, challenges, and future directions," Appl. Sci., vol. 15, no. 4, p. 1911, 2025, doi: 10.3390/app15041911.

[50] O. Hakimi, H. Liu, O. Abudayyeh, A. Houshyar, M. Almatared, and A. Alhawiti, "Data fusion for smart civil infrastructure management: A conceptual digital twin framework," Buildings, vol. 13, no. 11, p. 2725, 2023, doi: 10.3390/buildings13112725.